Hindawi
International Journal of Aerospace Engineering
Volume 2017, Article ID 1326309, 8 pages
https://doi.org/10.1155/2017/1326309

Research Article

The Application Research of Inverse Finite Element Method for Frame Deformation Estimation

Yong Zhao,[1] Hong Bao,[1] Xuechao Duan,[1] and Hongmei Fang[2]

[1]*Key Laboratory of Electronic Equipment Structure Design of Ministry of Education, Xidian University, Xi'an 710071, China*
[2]*Nanjing Research Institute of Electronics Technology, Nanjing 210039, China*

Correspondence should be addressed to Hong Bao; hbao@xidian.edu.cn

Received 6 February 2017; Revised 16 July 2017; Accepted 23 August 2017; Published 5 November 2017

Academic Editor: Vaios Lappas

A frame deformation estimation algorithm is investigated for the purpose of real-time control and health monitoring of flexible lightweight aerospace structures. The inverse finite element method (iFEM) for beam deformation estimation was recently proposed by Gherlone and his collaborators. The methodology uses a least squares principle involving section strains of Timoshenko theory for stretching, torsion, bending, and transverse shearing. The proposed methodology is based on stain-displacement relations only, without invoking force equilibrium. Thus, the displacement fields can be reconstructed without the knowledge of structural mode shapes, material properties, and applied loading. In this paper, the number of the locations where the section strains are evaluated in the iFEM is discussed firstly, and the algorithm is subsequently investigated through a simple supplied beam and an experimental aluminum wing-like frame model in the loading case of end-node force. The estimation results from the iFEM are compared with reference displacements from optical measurement and computational analysis, and the accuracy of the algorithm estimation is quantified by the root-mean-square error and percentage difference error.

1. Introduction

Aircraft flexible wings with embedded conformal antennas and large frame structures that carry antennas require accurate real-time deformation estimation to provide feedback for their actuation and control systems [1–3]. Using the measured strain to reconstruct the shape of the structure is a key technology in the accurate real-time deformation estimation, which has been studied by many researchers.

The computation of the displacement field of the deformed structure is commonly performed on the basis of strain data measured in real time by a network of strain gauges [4–6]. For example, fiber Bragg grating (FBG) sensors have been extensively researched for deformation estimation due to their lightness, accuracy, and easy embedment. The strategies that reconstruct the deformed shape displacement field of the structure with in situ strain data can be divided into two kinds. One of the two kinds trains the mapping relation between the displacement field and the measured strain by model learning algorithms, for example, neural network model and fuzzy network algorithm [7, 8]. When the training system has enough measured strains and displacement field data of the structure, a certain relation matrix can be determined and the stable relationship between the measured strain and the displacement field can be obtained. But the strategy requires a large number of training data, and the mapping relation is easy to fail when the actual loading is beyond the range of the training cases.

The other establishes the mapping relation between the displacement field and in situ strain data without the model learning. In the literature [9–11], the global or piecewise continuous basis function methods were employed to fit the surface-measured strain into the structure strain field, and then, the structure deformation displacement was obtained from the strain-displacement relationship. These methods are easy to implement, but the reconstruction accuracy of deformation estimation depends on the appropriate selection of basis function and weight coefficients. Mode shapes have been used as basis function in [12, 13]. The deformation displacements are reconstructed from measured strains by using the modal transformation method. However, there exist the following disadvantages in this method. (1) The detailed

material elasticity and inertial parameters are needed to precisely construct mode shapes. (2) The accuracy of deformation reconstruction is severely limited to the modeling precision of the structure, and it is quite difficult to precisely model the complex structure. Maincon [14] developed a finite element-based methodology involving an inverse interpolation formulation that employs the surface-measured strain to determine the loads and structural response of aerospace vehicles, while this algorithm needs an appropriate quality function to adapt the different loading cases and this function is constructed based on a mass of computer simulation and experimental statistics.

Based on the Euler-Bernoulli beam equation, Jute et al. evaluated the deflection of beam by the integration of discretely measured strains directly [15]. The algorithm applied the classical beam equation and piecewise continuous polynomials to approximate beam curvature through integration. Derkevorkian et al. [16] compared the algorithm with the modal transformation method and demonstrated the additional benefits of the algorithm to achieve a robust method for monitoring ultralightweight flying wings or next-generation commercial airplanes. Though this one-dimensional scheme has displayed high accuracy in predicting deflection, it fails to estimate the element deformation under multidimensional complex loads.

Tessler and Spangler [17] proposed the inverse finite methodology (iFEM), which can be used to reconstruct the displacement field of shear-deformable structures, not only beam structure but also plate and shell structures. The main idea is reconstructing a three-dimensional displacement field of beam structure from the surface-measured strains according to a least squares approach. Due to the fact that only the displacement-strain relationship is used, the deformation reconstruction can be accomplished by the methodology without the prior knowledge of loads, materials, and inertial and damping properties. To model arbitrary plate and shell structures [18, 19], Tessler and his partners developed the iFEM algorithm using the first-order shear deformation theory and a three-node inverse shell element. FBG sensors were applied to measure the surface strains on the slender beams, and then, the deformed displacement was reconstructed by using an iFEM shell model.

The beam-deformed displacement and cross-sectional torsion were reconstructed by Gherlone et al. who employed the inverse finite element formulation to achieve high reconstruction accuracy of deformed displacement [20–21]. The authors first used the Timoshenko beam theory to model the beam kinematic accurately, then used the C^0 or C^1 inverse frame elements and least squares formulation to establish the relationship between the measured strain and the arbitrary node displacement field of the beam element with no prior knowledge of the finite element model and loads. The reconstruction equation is nonsingular when the boundary conditions are applied; that is, the status of one end node of the beam element must be known. As the displacement field of the beam element in iFEM is constructed based on an isotropic straight beam structure, whose cross section is invariable along the whole beam, the deformation of the tapered beam cannot be estimated. Meanwhile, in view of different load cases, the authors discussed different types of shape functions that are used to interpolate the kinematic variables in the beam element; then, the number of surface strain measurements and the deformation reconstruction equation are confirmed. Unfortunately, the minimum number of locations where the section strains are evaluated, which is critical for obtaining a correct solution to the algorithm, is not discussed clearly in different load cases. If the minimum number of the locations where the section strains are evaluated is inappropriately set, the solution will be nonunique; that is, the reconstructed displacement may be incorrect.

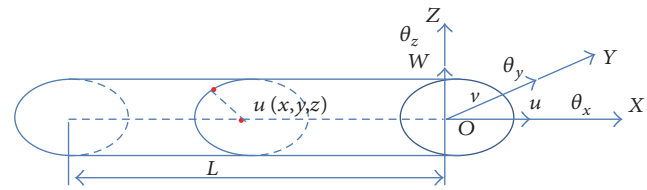

Figure 1: Beam geometry and kinematic variables.

The contribution of this paper is twofold. (i) The relationship between the loading case and the number of the section strain locations is discussed in detail, and the following conclusions are verified; on the one hand, the minimum number of locations should be 2 in the loading case of end-node forces; on the other hand, the minimum number should be 3 under the uniform distributed loading. (ii) In order to examine the minimum number which is 2, estimation studies are carried on a beam structure and a wing-like three-dimensional frame structure, in the loading case of end-node force. Six fiber optic strain sensors are placed at two nodes of each beam to capture in situ strain dates. To assess the estimation error of the iFEM algorithm, the RMS and difference percent parameters are employed.

2. iFEM Algorithms for Beam Estimation

A beam deflection estimation algorithm was developed by Gherlone and his collaborators [20]. In the algorithm, the Timoshenko beam theory is first used to analyze the expression of the displacement field in a straight beam element (Figure 1).

$$\begin{aligned} u_x(x,y,z) &= u(x) + z\theta_y(x) - y\theta_z(x), \\ v_y(x,y,z) &= v(x) - z\theta_x(x), \\ u_z(x,y,z) &= w(x) + y\theta_x(x), \end{aligned} \tag{1}$$

where u_x, v_y, and w_z are the point displacements along the x, y, and z axes, respectively. $u(x)$, $v(x)$, and $w(x)$ denote the displacements at $y = z = 0$; $\theta_x(x)$, $\theta_y(x)$, and $\theta_z(x)$ are the rotations about the three coordinate axes. The six kinematic variables in the middle axes can be grouped in vector form as follows:

$$\mathbf{u} = \{u, v, w, \theta_x, \theta_y, \theta_z\}^T. \tag{2}$$

The arbitrary section strains $\mathbf{e}(\mathbf{u}) = [e_1, e_2, e_3, e_4, e_5, e_6]^T$ can be obtained by (1).

$$\begin{aligned} e_1(x) &= u_x(x), \\ e_2(x) &= \theta_{y,x}(x), \\ e_3(x) &= -\theta_{z,x}(x), \\ e_4(x) &= w_x(x) + \theta_y(x), \\ e_5(x) &= v_x(x) - \theta_z(x), \\ e_6(x) &= \theta_{x,x}(x). \end{aligned} \tag{3}$$

The six kinematic variables $\mathbf{u}$ can be interpolated by the right shape functions

$$\mathbf{u} = \mathbf{N}(x)\mathbf{u}^{\mathbf{e}}, \tag{4}$$

where $\mathbf{N}(x)$ and $\mathbf{u}^{\mathbf{e}}$ denote the shape function and nodal degrees of freedom, respectively. Substituting (4) into (3) gives arbitrary section strains in terms of the nodal degrees of freedom as follows:

$$\mathbf{e}(\mathbf{u}) = \mathbf{B}(\mathbf{x})\mathbf{u}^{\mathbf{e}}, \tag{5}$$

where the matrix $\mathbf{B}(\mathbf{x}) = [B_1(\mathbf{x}), B_2(\mathbf{x}), \ldots, B_6(\mathbf{x})]$ contains the derivatives of the shape functions $\mathbf{N}(x)$. Once the section strains $\mathbf{e}(\mathbf{u})$ are obtained, the nodal displacement $\mathbf{u}^{\mathbf{e}}$ is determined; then, the kinematic variables $\mathbf{u}$ can be acquired by (4). However, the section strains $\mathbf{e}(\mathbf{u})$ are derived from the kinematic variables $\boldsymbol{u}$ theoretically, rather than the strain measurements. So, iFEM uses in situ section strains $\mathbf{e}^{\boldsymbol{\epsilon}}$ computed from the measured strains to replace $\mathbf{e}(\mathbf{u})$ when the least squares error function $\boldsymbol{\varphi}(\mathbf{u})$ reaches the minimum.

$$\boldsymbol{\varphi}(\mathbf{u}) = \|\mathbf{e}(\mathbf{u}) - \mathbf{e}^{\boldsymbol{\epsilon}}\|^2, \quad \mathbf{e}^{\boldsymbol{\epsilon}} = [\mathbf{e}_1^{\boldsymbol{\epsilon}}, \mathbf{e}_2^{\boldsymbol{\epsilon}}, \mathbf{e}_3^{\boldsymbol{\epsilon}}, \mathbf{e}_4^{\boldsymbol{\epsilon}}, \mathbf{e}_5^{\boldsymbol{\epsilon}}, \mathbf{e}_6^{\boldsymbol{\epsilon}}]^T. \tag{6}$$

In view of the effect of the axial stretching, bending, twisting, and transverse shearing, the improved least squares error functional $\boldsymbol{\varphi}^{\mathbf{e}}(\mathbf{u})$ is obtained by the dot product of the weighting coefficient vector $\mathbf{W}$ and the original vector $\boldsymbol{\varphi}(\mathbf{u}) = \{\varphi_k^e\}$.

$$\begin{aligned} \mathbf{W} &= \{w_k\} = \left\{ w_1^0, w_2^0\left(\frac{I_y^e}{A^e}\right), w_3^0\left(\frac{I_z^e}{A^e}\right), w_4^0, w_5^0, w_6^0\left(\frac{I_p^e}{A^e}\right) \right\}, \\ \boldsymbol{\varphi}^{\mathbf{e}}(\mathbf{u}) &= \mathbf{W} \cdot \boldsymbol{\varphi}(\mathbf{u}), \\ \varphi_k^e &= \frac{L}{n}\sum_{i=1}^{n} [e_k(x_i) - e_k^{\varepsilon}(x_i)]^2, \quad (k = 1, 2, \ldots, 6), \end{aligned} \tag{7}$$

where $w_k^0 (k = 1, 2, \ldots, 6)$ denote dimensionless weighting coefficients whose initial values are identically set as 1; A^e, I_y^e and I_z^e, and I_p^e are, respectively, the cross-sectional area, second moments of the area according to the y- and z-axes, and polar moment of the area of the beam element. L is the length of the beam element; $x_i (0 \le x_i \le L)$ and n are, respectively, the axial coordinate of the locations where the section strains are evaluated and the number of locations, that is, the axial coordinate of sections where section strains are distributed in, and the number of sections.

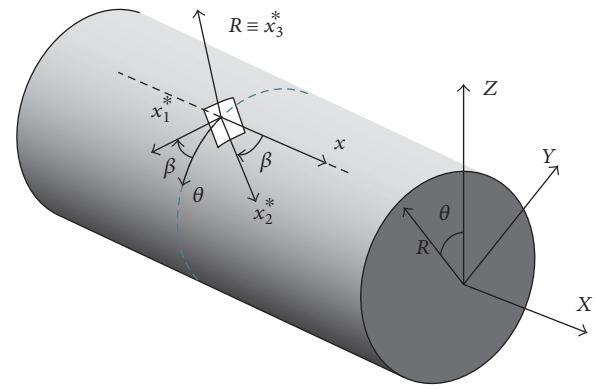

Figure 2: Location and coordinates of a strain gauge placed on the beam external surface.

For a straight beam member of constant circle cross section, the in situ section strains at $x = x_i$, $\mathbf{e}^{\boldsymbol{\epsilon}}(x_i) = [e_1^{\varepsilon}(x_i), e_2^{\varepsilon}(x_i), \ldots, e_6^{\varepsilon}(x_i)]^T$, could be derived from the measured strains of the beam surface with appropriate strain-tensor transformations from the (θ, x, r) to (x_X, x_Y, x_Z) coordinates [22].

$$\begin{aligned} \varepsilon_2^*(x_i, \theta, \beta) = {} & e_1^{\varepsilon}(x_i)\left(c_\beta^2 - \nu s_\beta^2\right) + e_2^{\varepsilon}(x_i)\left(c_\beta^2 - \nu s_\beta^2\right)s_\theta R \\ & + e_3^{\varepsilon}(x_i)\left(c_\beta^2 - \nu s_\beta^2\right)c_\theta R + e_4^{\varepsilon}(x_i)c_\beta s_\beta c_\theta \\ & - e_5^{\varepsilon}(x_i)c_\beta s_\beta s_\theta + e_6^{\varepsilon}(x_i)c_\beta s_\beta R, \end{aligned} \tag{8}$$

with $c_\beta \equiv \cos\beta$, $s_\beta \equiv \sin\beta$, $c_\theta \equiv \cos\theta$, and $s_\theta \equiv \sin\theta$.

In (8), ν is the Poisson ratio, $\varepsilon_2^*(x_i, \theta, \beta)$ is the in situ strains that are obtained from strain sensors. R denotes the radius of the beam cross section (Figure 2).

Substituting (5) into (7) results in the following quadratic form:

$$\boldsymbol{\varphi}^{\mathbf{e}}(\mathbf{u}) = \frac{1}{2}(\mathbf{u}^{\mathbf{e}})^{\mathbf{T}}\mathbf{k}^{\mathbf{e}}\mathbf{u}^{\mathbf{e}} - (\mathbf{u}^{\mathbf{e}})^{\mathbf{T}}\mathbf{k}^{\mathbf{e}} + \mathbf{c}^{\mathbf{e}}. \tag{9}$$

Herein, $\mathbf{c}^{\mathbf{e}}$ is a constant, and $\mathbf{k}^{\mathbf{e}}$ and $\mathbf{f}^{\mathbf{e}}$ are indicated as follows:

$$\begin{aligned} \mathbf{k}^{\mathbf{e}} &= \sum_{k=1}^{6} w_k k_k^e, \quad k_k^e = \frac{L}{n}\sum_{i=1}^{n}\left[B_k^T(x_i)B_k(x_i)\right], \\ \mathbf{f}^{\mathbf{e}} &= \sum_{k=1}^{6} w_k f_k^e, \quad f_k^e = \frac{L}{n}\sum_{i=1}^{n}\left[B_k^T(x_i)e_k^{\varepsilon}(x_i)\right]. \end{aligned} \tag{10}$$

Finally, the relationship between the deformation and in situ section strains, shown in (11), can be confirmed when the minimization of functional $\boldsymbol{\varphi}^{\mathbf{e}}(\mathbf{u})$ is performed.

$$\mathbf{k}^{\mathbf{e}}\mathbf{u}^{\mathbf{e}} = \mathbf{f}^{\mathbf{e}}. \tag{11}$$

Once the appropriate shape functions and the problem-dependent displacement boundary conditions (e.g., setting the displacement of one end point to zero, which means that one of end nodes of the beam is fixed) are given, $\mathbf{u}^{\mathbf{e}}$ can be derived from a nonsingular system, and the vector $\mathbf{f}^{\mathbf{e}}$ depends on the measured strain values that change during

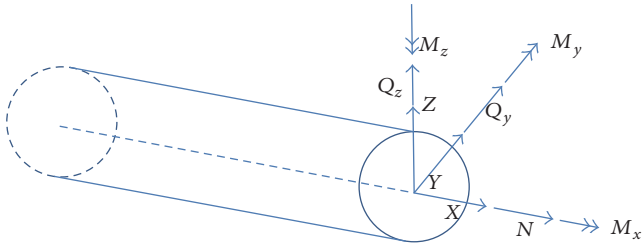

Figure 3: Beam section forces and moments.

deformation. Once the nodal degrees of freedom $\mathbf{u}^e$ are confirmed, the displacements and rotations of every node along the centroid axis of the beam element are obtained by (4) and the deformed shape of the whole beam can be reconstructed by (1).

3. Minimum Number of the Section Strain Location Selection

Although the displacement shape function and the number of surface strain measurements in different loading cases have been discussed in [20, 21], n, the number of the sections where the section strains are distributed in, is not shown clearly. In (11), once the problem-dependent displacement boundary conditions are determined, the nonsingularity of the equation will depend on the selection of n. In our investigation, it is found that n can be determined by a specific loading case. More specifically, the orders of the section forces and the moments can be obtained by the loading case, which determines the order of the section strains. With the value of the section strain order, n is determined immediately.

With the equilibrium equations (12), the section forces (N, Q_y, and Q_z) and moments (M_x, M_y, and M_z) can be obtained by the load concentrations $q_x(x)$, $q_y(x)$, and $q_z(x)$ along the x, y, and z directions (Figure 3).

$$\begin{aligned} N_x + q_x(x) &= 0, \\ Q_{y,x} + q_y(x) &= 0, \\ Q_{z,x} + q_z(x) &= 0, \\ M_{x,x} &= 0, \\ M_{y,x} - Q_z &= 0, \\ M_{z,x} - Q_y &= 0. \end{aligned} \tag{12}$$

The relationship between section forces and moments and the section strains $e_i\,(i = 1, 2, \ldots, 6)$ can be interpreted as the following constitutive equations:

$$\begin{aligned} N &= A_x e_1, \\ M_x &= J_x e_6, \\ Q_y &= G_y e_5, \\ M_y &= D_y e_2, \\ Q_z &= G_z e_4, \\ M_z &= D_z e_3. \end{aligned} \tag{13}$$

where $A_x \equiv EA$ is the axial rigidity; $G_y \equiv k_y^2 GA$ and $G_z \equiv k_z^2 GA$ are the shear rigidities, with k_y^2 and k_z^2 denoting the shear correction factors; and $J_x \equiv GI_p$ and $D_y \equiv EI_y$ and $D_z \equiv EI_z$ are, respectively, the torsional rigidity and the bending rigidities. For the uniform section beam element, parameters mentioned above are constant. Then, the order of the section strains e_i will be identical to that of the section forces and moments.

Substituting (13) into (12) gives the relationship between the section strains and the loads as follows:

$$\begin{aligned} e_1 &= \frac{N}{A_x} = \frac{\int(-q_x(x))dx}{A_x}, \\ e_2 &= \frac{M_y}{D_y} = \frac{\int Q_z dx}{D_y} = \frac{\int\int(-q_z(x))dxdx}{D_y}, \\ e_3 &= \frac{M_z}{D_z} = \frac{\int Q_y dx}{D_z} = \frac{\int\int(-q_y(x))dxdx}{D_z}, \\ e_4 &= \frac{Q_z}{G_z} = \frac{\int(-q_z(x))dx}{G_z}, \\ e_5 &= \frac{Q_y}{G_y} = \frac{\int(-q_y(x))dx}{G_y}, \\ e_6 &= \frac{M_x}{J_x} = \frac{\int 0dx}{J_x} = c_1. \end{aligned} \tag{14}$$

In most cases, the load in the x direction is zero, that is, $q_x(x) = 0$; then,

$$e_1 = \frac{\int(-q_x(x))dx}{A_x} = \frac{\int 0dx}{A_x} = c_2. \tag{15}$$

The section strains e_1 and e_6 are constant in (14) and (15), and the order of the residual section strains, e_2, e_3, e_4, and e_5, will be discussed as the following two loading cases.

Consider a beam element loaded by the end-node forces, $q_y(x)$ and $q_z(x)$ are zero along the x-axis. Then, e_2, e_3, e_4, and e_5 are determined by (14).

$$\begin{aligned} e_2 &= \frac{\int\int(-q_z(x))dxdx}{D_y} = \frac{\int\int 0dxdx}{D_y} = a_1 x + b_1, \\ e_3 &= \frac{\int\int(-q_y(x))dxdx}{D_z} = \frac{\int\int 0dxdx}{D_z} = a_2 x + b_2, \\ e_4 &= \frac{\int(-q_z(x))dx}{G_z} = \frac{\int 0dx}{G_z} = a_3, \\ e_5 &= \frac{\int(-q_y(x))dx}{G_y} = \frac{\int 0dx}{G_y} = a_4. \end{aligned} \tag{16}$$

where a_1, a_2, a_3, a_4, b_1, and b_2 are unknown constant parameters.

As in (15), the highest order of the section strains $\mathbf{e}(\mathbf{u})$ is linear (e_2, e_3), which means that the distribution of the bending moments is a skew line, that the corresponding errors in (7) can be obtained from the shaded area between two skew lines, and that each line can be confirmed by two different nodes, that is, two section strains in different sections

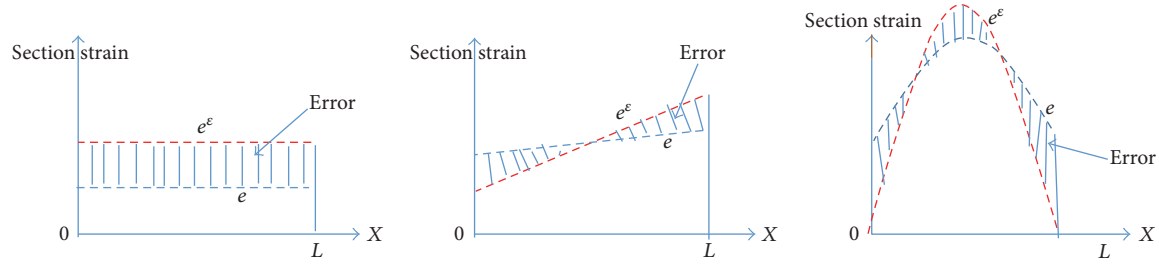

(a) Constant section strain (b) Linear section strain (c) Quadratic section strain

FIGURE 4: Distribution and error of section strains in different orders. e^ε is a section strain in $\mathbf{e}^\epsilon$ computed from surface strain measurements by (8). e is a section strain in $\mathbf{e}(\mathbf{u})$ deduced by (3).

(Figure 4(a)). Thus, $n = 2$ for e_2 and e_3 in (7). Meanwhile, the other section strains, e_1, e_4, e_5, and e_6, are constant, which means that their distributions are lines parallel to the x-axis, that the associative errors in (7) can be obtained from the shaded area between two parallel lines, and that every line can be confirmed by one node, that is, one section strain (Figure 4(b)). Thus, the number of the sections where section strains are distributed is $n = 1$. Finally, the number of the sections, n, is 2 in (7) and (10) in the loading case of end-node force and moments.

Another case is the beam element loaded by uniformly distributed forces, $q_y(x)$ and $q_z(x)$ are constant along the x-axis, and the order of the section strains e_2, e_3, e_4, and e_5 can be deduced as follows.

Assumption: $q_y(x) = d_1$, $q_z(x) = d_2$.

Then,

$$
\begin{aligned}
e_2 &= \frac{\int\int(-q_z(x))dxdx}{D_y} = \frac{\int\int(-d_2)dxdx}{D_y} = \frac{-d_2}{2D_y}x^2 + d_3x + d_4,\\
e_3 &= \frac{\int\int(-q_z(x))dxdx}{D_z} = \frac{\int\int(-d_1)dxdx}{D_z} = \frac{-d_1}{2D_z}x^2 + d_5x + d_6,\\
e_4 &= \frac{\int(-q_z(x))dx}{G_z} = \frac{\int(-d_2)dx}{G_z} = \frac{-d_2x}{G_z} + d_7,\\
e_5 &= \frac{\int(-q_y(x))dx}{G_y} = \frac{\int(-d_1)dx}{G_y} = \frac{-d_1x}{G_y} + d_8.
\end{aligned}
\tag{17}
$$

Herein, d_i $(i = 1, \ldots, 8)$ are unknown constant parameters. The highest order of the section strains $\mathbf{e}(\mathbf{u})$ is quadratic (e_2, e_3), and then, the distribution of the bending moments is a parabola. The corresponding errors in (7) can be obtained from the shaded area between two parabolas which are confirmed by three different nodes (Figure 4(c)), that is, three section strains in three different sections. Thus, $n = 3$ for e_2 and e_3 in (7). Meanwhile, e_4 and e_5 are linear, where the distribution is a skew line, and e_1 and e_6 are constant. Similar to the loading case of end-node force, the corresponding numbers of sections are 1 and 2, respectively. Finally, the number of the sections, n, is 3 in (7) and (10) in the loading case of uniformly distributed forces.

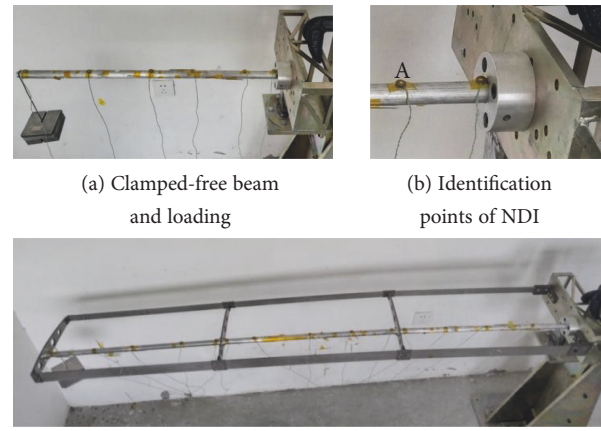

(a) Clamped-free beam and loading (b) Identification points of NDI

(c) Frame structure and loading

FIGURE 5: Loading case and the distributions of NDI identification points.

4. Verification

A simple cantilevered solid beam and a three-dimensional frame structure were subjected to the end-node static loads to assess the iFEM potential for the flexible wing deformation estimation. The beam and frame structures were made of 6061-T6 aluminum alloy. The Young's modulus is $E = 73000$ Mpa, the Poisson ratio is $\nu = 0.3$, and its density is $\rho = 2712.63\text{kg/m}^3$. The frame was composed of three solid beams and middle plates; the span of each beam $L = 640$ mm and the radius $R = 10$ mm (see Figure 5). For the solid circular cross section, the shear correction factors are $k_y^2 = k_z^2 = 0.887$ [21]. In our verification, every whole solid beam is regarded as one beam element. Accordingly, the principle axis of frame structure is divided into three elements.

The experimentally measured surface strains are obtained by fiber optic strain sensors. Displacement measurements are captured by 3D optical measurement instruction (NDI, Optotrak Certus), which determines the position of the identification point by using three CCD cameras to capture the infrared lights emitted by position sensors (Figure 6). The instruction is also used to assess the iFEM-recovered deflections, where the accuracy of the NDI is 0.1 mm. A position sensor was placed as close as possible to

Figure 6: Static test setup. The single beam (A), frame structure (B), and NDI Optotrak Certus (C).

Table 1: Optical fiber sensor location in one element.

$e^{\varepsilon_1}(x,\theta,\beta)$	$e^{\varepsilon_2}(x,\theta,\beta)$	$e^{\varepsilon_3}(x,\theta,\beta)$	$e^{\varepsilon_4}(x,\theta,\beta)$	$e^{\varepsilon_5}(x,\theta,\beta)$	$e^{\varepsilon_6}(x,\theta,\beta)$
$(L/2,-2\pi/3,0)$	$(L/2,0,0)$	$(L/2,2\pi/3,0)$	$(4L/5,-2\pi/3,0)$	$(4L/5,0,\pi/4)$	$(4L/5,2\pi/3,0)$

Table 2: Loading case for the clamped-free beam. Max deflections are captured from NDI.

	Case 1	Case 2	Case 3	Case 4	Case 5
Loads	5 N	15 N	37 N	41 N	68 N
Max deflection in Y	−0.79 mm	−2.5 mm	−6.11 mm	−6.82 mm	−10.96 mm
RMS in Y	0.05 mm	0.16 mm	0.32 mm	0.33 mm	0.42 mm
%Diff(v) in Y	6%	6.4%	5.2%	4.8%	3.8%

the beam root to verify the effectiveness of the clamping arrangement. The force is achieved by placing several weights on a pothook.

For the frame structure, each beam is regarded as an element and the optical fiber sensor location scheme used for each element is identical. For the end-node static loads, the displacement field of the whole beam element is interpolated by C^0 continuous shape function and the number of required strain sensors is 6 (see [21]). As the radius of the beam element is small ($R = 10$ mm) and the grid length of every fiber grating sensor is 10 mm, it is difficult to stick the six strain gauges on one section; six fiber optic strain gauges are placed on two different sections along the beam (Table 1).

The accuracy of the reconstitution is assessed by root-mean-square (RMS) and percentage difference (%Diff).

$$\begin{aligned} \mathrm{RMS} &= \sqrt[2]{\sum_{i=1}^{m}\left(\tau^{\mathrm{iFEM}}(x_i)-\tau^{\mathrm{NDI}}(x_i)\right)^2}, \\ \%\mathrm{Diff}(\tau) &= 100 * \left[\frac{\mathrm{RMS}}{\max\left|\tau^{\mathrm{NDI}}(x_i)\right|}\right], \end{aligned} \tag{18}$$

where $\tau = (v, w)$ is the deformation displacement along the y- or z-axis and m is the number of deflection shape displacement measurement identification points of NDI (Figure 5(b)A) in the structure. For the beam, $m = 6$ (Figure 5(a)), and for the frame, $m = 14$ (Figure 5(c)). The superscript "iFEM" refers to the reconstitution by iFEM while "NDI" refers to the experimental measure from 3D optical measurement instruction; x_i is the ith location along the axis where the displacement u is measured.

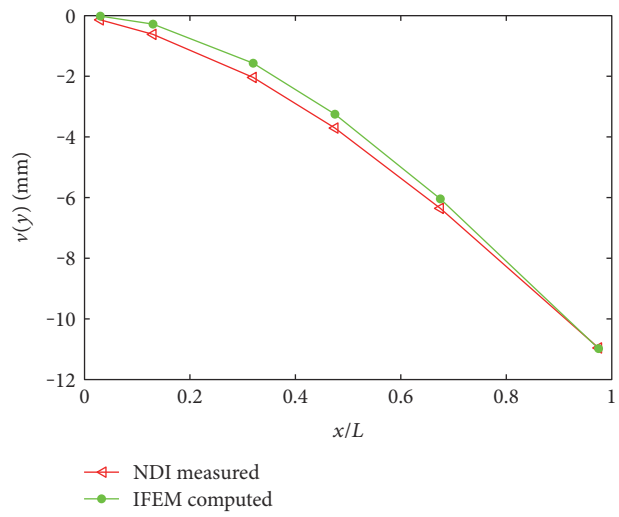

Figure 7: Comparison of iFEM reconstruction for a beam to NDI measurement in Y.

At first, five different vertical force cases (Table 2) were applied at the free end of the beam (Figure 5(a)). Figure 7 shows the comparison between iFEM reconstruction and NDI measurement along the beam axis in force direction, for the loading case 68 N. Symbol x/L indicates the location of identification point along the beam surface. Zero means identification point at the clamped end node, and 1 means identification point at the free end node. $v(y)$ indicates the corresponding displacement in force direction.

Table 3: Loading case for the frame structure. Max deflections are captured from NDI.

	Case 1	Case 2	Case 3	Case 4	Case 5
Loads	18 N	23 N	35 N	45.5 N	68 N
Max deflection in Y	16.31 mm	20.5 mm	31.2 mm	41.3 mm	62.8 mm
RMS in Y	0.22 mm	0.49 mm	2.0 mm	3.3 mm	6.8 mm
%Diff(v) in Y	1.3%	2.4%	6.4%	8.1%	10.9%
Max deflection in Z	2.53 mm	3.23 mm	5.1 mm	6.5 mm	10.2 mm
RMS in Z	0.32 mm	0.41 mm	0.73 mm	0.75 mm	1.1 mm
%Diff(w) in Z	12.6%	12.8%	14.6%	11.5%	10.8%

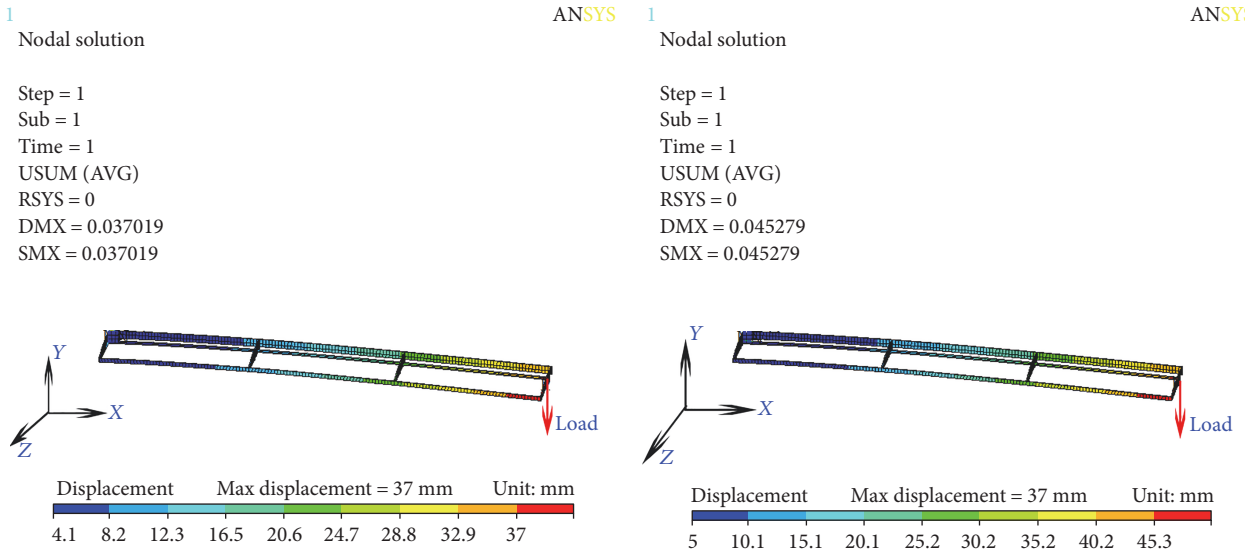

(a) Contour plot of iFEM reconstruction

(b) Contour plot of NDI measurement

Figure 8: Comparison of iFEM reconstruction for a frame to NDI measurement.

For the frame structure, five different vertical force cases (Table 3) were applied at the free end of the frame (Figure 5(c)). The two deformation contour plots of the frame are plotted by high-fidelity direct FE analysis (ANSYS 12.0), which shows the comparison between iFEM reconstruction and NDI measurement along the beam axis in force direction, for the loading case 45.5 N (Figure 8). The deformation unit in the two figures is meter.

It is seen from the preceding results that the iFEM methodology shows a good potential as a reliable estimation technique. The estimation results gained from the iFEM algorithm have a better approximation to the NDI measurement results. For the beam test, the accuracy of the reconstitution assessed by percentage difference does not exceed 6.4% and the error brings down with the loading increase. For the frame test in the loading case of 18 N, the percentage difference is 1.3%, but the difference grows up with the loading increase; especially from the loading case 23 N to 35 N, the difference increases 4%. The cause for this phenomenon is that the gripper of the frame structure is not very stable, which leads to the fact that the gap spacing between the frame and its carrier grows up with the loading increase that has a great influence on the boundary conditions.

5. Conclusion

This study investigates the application potential of the iFEM algorithm for the flexible wing and other frame structures. This method employs the in situ strain measurements and proper displacement shape function to estimate the deformation shape of the beam and frame structure, without the need to know the applied loads and material properties and to use modal shapes. When the boundary conditions of the reconstruction equation and the shape function are determined, the deformation shape will be accurately estimated in a nonsingular system. Although the boundary conditions are known in hypothesis, the number of location where the section strains are evaluated is not shown clearly; thereby, the singularity of the equation will be influenced.

This paper discusses the minimum number of location where the section strains are evaluated with the loading case, using equilibrium equations in detail, and verifies the result that for the loading case of end-node force, the number is 2. The results of the static loads in the beam and the frame model show that the iFEM algorithm has a good potential for the flexible frame structure estimation; especially for a simply supported beam, the accuracy of the estimation by

iFEM is around 6%, and for the frame structure in small load (18 N), the accuracy reaches up to 1.3%, while as the gripper of the frame is not firm enough, the estimation accuracy brings down with the loading increase. So, the next work is to explore the technology that reduces the influence of the gap spacing of the frame gripper on accuracy of the frame deformation estimation.

Conflicts of Interest

The authors declare that there is no conflict of interest regarding the publication of this paper.

Acknowledgments

This work was financially supported by the National Natural Science Foundation of China (Grants 51675398 and 51775401), the National Key Basic Research Program of China (Grant 2015CB857100), and the CAS "Light of West China" Program (no. 2016-QNXZ-A-7).

References

[1] W. Akl, S. Poh, and A. Baz, "Wireless and distributed sensing of the shape of morphing structures," *Sensors and Actuators A*, vol. 140, no. 1, pp. 94–102, 2007.

[2] Z. Mao and M. Todd, "Comparison of shape reconstruction strategies in a complex flexible structure," *Proceedings of SPIE*, vol. 6932, article 69320H, 2008.

[3] P. David, J. Kenneth, and G. Vladimir, "Distortion measurement and compensation in a synthetic aperture radar phased-array antenna," in *2010 14th International Symposium on Antenna Technology and Applied Electromagnetics and the American Electromagnetics Conference (ANTEM-AMERRM)*, pp. 1–5, Ottawa, ON, Canada, 2010.

[4] W. Yin, T. Fu, J. Liu, and J. Leng, "Structural shape sensing for variable camber wing using FBG sensors," in *Proceedings of SPIE 7292, sensors and smart structures technologies for civil, mechanical, and aerospace systems*, vol. 7292, p. 72921H, San Diego, CA, USA, March 2009.

[5] S. Rapp, L. H. Kang, J. H. Han, U. C. Mueller, and H. Baier, "Displacement field estimating for a two-dimensional structure using fiber Bragg grating sensors," *Smart Materials and Structures*, vol. 18, no. 2, article 025006, 2009.

[6] L. Kang, D. Kim, and J. Han, "Estimation of dynamic structural displacements using fiber Bragg grating strain sensors," *Journal of Sound and Vibration*, vol. 305, no. 3, pp. 534–542, 2007.

[7] D. Ganotra, J. Joseph, and K. Singh, "Object reconstruction in multilayer neural network based profilometry using grating structure comprising two regions with different spatial periods," *Optics and Lasers in Engineering*, vol. 42, no. 2, pp. 179–192, 2004.

[8] Z. Yong, B. Hong, D. Xuechao, and F. Hongmei, "Research of situ strain of measuring flexible truss deformation based on fuzzy network method," in *2016 International Conference on Computer Engineering, Information Science & Application Technology (ICCIA 2016)*, pp. 401–410, Guilin, China, 2016.

[9] G. Foss and E. Haugse, "Using modal test results to develop strain to displacement transformation," in *Proc. 13th The International Society for Optical Engineering*, pp. 112–118, Nashville, TN, February 1995.

[10] S. L. Peter, J. A. Mauro, and W. H. Nesbitt, "Investigation of filtering techniques applied to the dynamic estimation problem," *Smart Materials and Structures*, vol. 10, no. 2, pp. 264–272, 2001.

[11] M. D. Todd and S. T. Vohra, "Shear deformation correction to transverse shape reconstruction from distributed strain measurements," *Journal of Sound and Vibration*, vol. 225, no. 3, pp. 581–594, 1999.

[12] B. B. Philip, H. Eric, and E. G. Ralph, "Structural shape identification from experimental strains using a modal transformation technique," in *4th AIAA/ASME/ASCE/AHS Structures, Structural Dynamics, and Materials Conference*, pp. 7–10, Norfolk, Virginia, April 7, 2003.

[13] H. I. Kim, L. H. Kang, and J. H. Han, "Shape estimation with distributed fiber Bragg grating sensors for rotating structures," *Smart Materials and Structures*, vol. 20, no. 3, pp. 35011–35021, 2011.

[14] P. Maincon, "2004 inverse FEM I: load and response estimates from measurements," in *Proceedings of 2nd International Conference on Structural Engineering, Mechanics and Computation*, pp. 967–971, Cape Town, 2004.

[15] C. Jute, W. Ko, and C. Stephens, "Deformed shape calculation of a full-scale wing using fiber optic strain data from a ground loads test," NASA Langley Research Center, Rept. TP-215975, Hampton, VA, USA, 2011.

[16] A. Derkevorkian, S. F. Masri, J. Alvarenga, H. Boussalis, J. Bakalyar, and W. L. Richards, "Strain-based deformation shape-estimation algorithm for control and monitoring applications," *AIAA Journal*, vol. 51, no. 9, pp. 2231–2240, 2013.

[17] A. Tessler and J. Spangler, "A variational principle for reconstruction of elastic deformations in shear deformable plates and shells," NASA Langley Research Center TM-212445, Hampton, VA, USA, 2003.

[18] A. Tessler and J. Spangler, "A least-squares variational method for full-field reconstruction of elastic deformations in shear-deformable plates and shells," *Computer Methods in Applied Mechanics and Engineering*, vol. 194, no. 2–5, pp. 327–339, 2005.

[19] C. C. Quach, S. L. Vazquez, A. Tessler, and J. P. Moore, "Structural anomaly detection using fiber optic sensors and inverse finite element method," in *AIAA Guidance, Navigation, and Control Conference and Exhibit*, San Francisco, CA, USA, 2005.

[20] M. Gherlone, P. Cerracchio, M. Mattone, M. Di Sciuva, and A. Tessler, "Dynamic shape reconstruction of three-dimensional frame structures using the inverse finite element method," NASA Langley Research Center TM-217315, Hampton, VA, USA, 2011.

[21] M. Gherlone, P. Cerracchio, M. Mattone, M. Di Sciuva, and A. Tessler, "Shape sensing of 3D frame structures using an inverse finite element method," *International Journal of Solids and Structures*, vol. 49, no. 22, pp. 3100–3112, 2012.

[22] A. I. Lurie, *Theory of Elasticity*, Springer-Verlag Berlin Heidelberg, New York, NY, USA, 2005.